

***Thermo-mechanical analysis
of SiC and FeCrAl cladding
behavior under a loss-of-
coolant accident***

**Nuclear Technology
Research and Development**

Approved for public release.
Distribution is unlimited.

***Prepared for
U.S. Department of Energy
Nuclear Technology Research and
Development Advanced Fuels Campaign
R. Sweet^{1,2}, A. Nelson¹ and B. D. Wirth^{1,2}***

¹Oak Ridge National Laboratory

²University of Tennessee Knoxville

September 12, 2018

M3NT-18OR020205032



DISCLAIMER

This information was prepared as an account of work sponsored by an agency of the U.S. Government. Neither the U.S. Government nor any agency thereof, nor any of their employees, makes any warranty, expressed or implied, or assumes any legal liability or responsibility for the accuracy, completeness, or usefulness, of any information, apparatus, product, or process disclosed, or represents that its use would not infringe privately owned rights. References herein to any specific commercial product, process, or service by trade name, trade mark, manufacturer, or otherwise, does not necessarily constitute or imply its endorsement, recommendation, or favoring by the U.S. Government or any agency thereof. The views and opinions of authors expressed herein do not necessarily state or reflect those of the U.S. Government or any agency thereof.

SUMMARY

Alternative cladding materials have been proposed to replace the currently used zirconium (Zr)-based alloys, in order to improve the accident tolerance of light water reactor (LWR) fuel. Of these materials, there is a particular focus on iron-chromium-aluminum (FeCrAl) alloys and silicon carbide composite materials that exhibit much slower oxidation kinetics in high-temperature steam than Zr-alloys. This behavior should decrease the energy release due to oxidation and allow the cladding to remain integral longer in the presence of high temperature steam, making accident mitigation more likely.

This analysis focused on modeling and comparing the integral thermo-mechanical performance of Zircaloy, FeCrAl, and SiC/SiC clad uranium dioxide fuel during transient reactor operation. Results from this analysis show a benefit of SiC/SiC and FeCrAl cladding with respect to the predicted maximum cladding hoop stress at failure for low (20 MWd/kgU) and medium (40 MWd/kgU) burnup fuel rods, as compared to Zircaloy. Future analysis efforts will incorporate improved failure models for the SiC/SiC and FeCrAl cladding, taking into account the temperature dependence of the proportional limit and ultimate tensile strength, respectively, and implementing improved models for high temperature oxidation.

TABLE OF CONTENTS

List of Figures	vi
1. INTRODUCTION	1
2. THERMO-MECHANICAL MODELING APPROACH	3
2.1 High-Temperature Constitutive Models.....	3
2.1.1 High-Temperature Thermal Creep Model.....	3
2.1.2 Cladding Plasticity and Failure Models	5
2.1.3 Oxidation Models	8
2.2 LOCA Operating Conditions.....	9
3. RESULTS	12
3.1 Steady-State Operation Results	12
3.2 LOCA Results	14
4. SUMMARY.....	17
5. REFERENCES.....	19

LIST OF TABLES

Table 1. Thermal Creep Parameters for FeCrAl Cladding.....	4
Table 2. High-Temperature Creep Parameters for Zircaloy-4 Cladding (Erbacher et al., 1982) [adapted from (Pastore et al., 2015)].....	4
Table 3. Phase Dependent Burst Stress Parameters for Zircaloy-4 (Erbacher et al., 1982)	8
Table 4. Fuel geometry specifications for 2D axisymmetric fuel performance analyses.....	10
Table 5. Loss-of-Coolant Accident Reactor and Fuel Properties	11

List of Figures

Figure 1. BISON simulation showing local temperature, creep strain, and area of cladding burst for Zircaloy cladding under LOCA conditions, as reproduced from (Pastore et al., 2015).	2
Figure 2. The thermal creep behavior for both the FeCrAl and the Zircaloy is divided into a separate low-temperature and high-temperature contribution with interpolation between the two regions.	5
Figure 3. BISON model predictions for the stress strain response of a FeCrAl subject to a simulated tensile test, as a function of test temperature. These simulations end when the ultimate tensile strength is reached.	6
Figure 4. Ultimate tensile strength of FeCrAl as a function of temperature showing two iterations of the model implemented in BISON for high temperatures (initial versus current), compared to a fit to available data performed by Gamble and co-workers (Gamble et al., 2017) and UTS data from (Yamamoto et al., 2015).	7
Figure 5. The power history of fuel rods in this LOCA analysis, (a) the Linear heat rate is divided into three regions: the initial ramp to operating power, constant operation at 20kW/m, and the reactor scram at the beginning of the transient conditions and the subsequent decay heat production. The axial power profile (b) is assumed to be constant for all three regions.	11
Figure 6. The average fuel temperature (a) for the SiC/SiC cladded fuel rods is much larger (~200 K) for much of the fuel utilization. The onset of gap closure (b) occurs much sooner for the Zircaloy cladded fuel rods than the SiC/SiC, while the FeCrAl cladded fuel rod does not experience gap closure up to 40 MWd/kgU.	13
Figure 7. The maximum cladding oxidation thickness for the Zircaloy versus FeCrAl cladding, as a function of burnup.	13
Figure 8. The maximum fuel centerline temperature (a) and the maximum cladding temperature (b) for all three cladding types as a function of time after the accident. The results from the TRACE simulation are (black line) included in b) to provide a comparison.	15
Figure 9. After the reactor is scrammed, the fuel contracts and the fuel cladding gap (a) is expanded. The Zircaloy cladding shows a much sharper increase in the gap thickness as the accident conditions progress. The maximum cladding hoop stress (b) is reduced as the accident conditions are initiated, however, as the accident progresses, the hoop stress in the FeCrAl and SiC/SiC cladding increases until failure.	15

1. INTRODUCTION

During a severe accident scenario with Zircaloy cladding, such as a beyond design basis loss-of-coolant-accident, as the reactor loses its capability to cool the fuel, fuel rod temperatures begin to increase. The radial temperature gradient inside the fuel rod rapidly decreases to a nearly uniform temperature distribution once the fission reaction is shutdown (Terrani et al., 2014). However, the average temperature begins to increase, quickly reaching temperatures sufficient to boil off the coolant. This reduces the coolant level in the core and eventually uncovers the fuel, also significantly reducing the heat transfer coefficient, further increasing the average fuel temperature. Eventually, if this increase in temperatures is unmitigated, then the cladding will begin to ‘balloon’, or deform outwards, due to the pressure differential between the interior of the fuel rod and the pressure remaining in the reactor pressure vessel. If this deformation persists, cladding burst can occur during these high temperature conditions from a combination of thermal creep and plasticity (Erbacher and Leistikow, 1987). If the temperature continues to increase further, the exothermic oxidation reaction of the Zircaloy cladding may become autocatalytic when the cladding temperature reaches $\sim 1200\text{ }^{\circ}\text{C}$ (Cathcart et al., 1977; Moalem and Olander, 1991). This produces large amounts of heat, consumes the cladding, and produces hydrogen gas (Hofmann, 1998). Within this study, the cladding performance for Zircaloy and candidate alternative materials under these conditions are targeted.

After the accident at the Fukushima Daiichi Nuclear Generating Station, the first large-scale nuclear accident in several decades, interest was renewed in identifying possible fuel-cladding systems with enhanced accident tolerance (Carmack et al., 2013), and developing them to commercialization. The operational goals for these candidate fuel systems include a reduced hydrogen generation rate, enhanced fission product retention, structural integrity in high temperature steam, and reduced fuel-cladding chemical and mechanical interaction. This work ultimately led to the identification, testing, and development of the iron-chromium-aluminum alloy and silicon carbide composite (SiC/SiC) cladding material.

In order to provide insight into how FeCrAl or SiC/SiC cladding will perform compared to Zircaloy in this environment, simulations have been performed after constructing and implementing constitutive relations, fuel rod geometries, and representative reactor conditions into the BISON fuel performance code.

While a number of situations can ultimately lead to fuel failure, the target of this analysis is the cladding behavior in the high-temperature environment sustained during a potential large-break loss-of-coolant (LBLOCA) accident. In this analysis, conditions from a mitigated LBLOCA are extended to compare the beyond-design-basis accident response of FeCrAl and SiC/SiC, as compared to standard Zircaloy cladding.

Traditionally, separate fuel performance codes are utilized to simulate the fuel rod behavior under steady-state and transient conditions either in conjunction with each other, or to provide a stand-alone analysis. Transitioning the state of the fuel rod from normal operation into the transient environment is necessary to evaluate the unique condition of the fuel at a variety of fuel burnups. To accomplish this, these simulation conditions contain long-term steady-state reactor operation

before transitioning into the accident scenario. This allows the state of the integral fuel rod at different specified burnups to be incorporated into the transient analysis.

Simulations of Zircaloy cladding behavior under LOCA conditions have been performed by Pastore and co-workers using the BISON fuel performance code (Pastore et al., 2015) with the purpose of comparing modeling predictions to the REBEKA cladding burst tests. Figure 1 shows azimuthally and axially varying temperatures on the cladding surface as well as the cladding creep strain, and the cladding elements determined to have ruptured. This analysis was performed using specifications from the REBEKA cladding burst test suite and demonstrate that the BISON fuel performance code has a framework in place to implement additional models and assess fuel and cladding behavior in transient conditions.

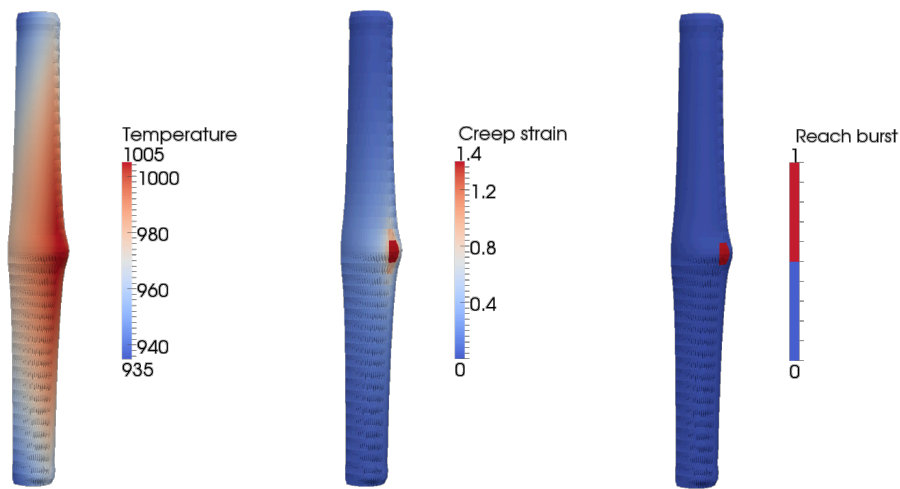


Figure 1. BISON simulation showing local temperature, creep strain, and area of cladding burst for Zircaloy cladding under LOCA conditions, as reproduced from (Pastore et al., 2015).

To accurately simulate the cladding behavior under a loss of coolant accident, several key models are needed. These include chemical and phase changes of the cladding alloy (such as oxidation), high-temperature constitutive behavior, and cladding rupture criteria.

2. THERMO-MECHANICAL MODELING APPROACH

BISON is a finite-element simulation tool for nuclear fuel elements that is based on the Multiphysics Object Oriented Simulation Environment (MOOSE) framework (Williamson et al., 2012). It utilizes a Jacobian-Free Newton-Krylov method to solve coupled systems of non-linear partial differential equations while leveraging the scalability of parallel computing. Because of the expandability of the MOOSE framework (Gaston et al., 2009), BISON can incorporate a host of materials as well as behavioral models for integral fuel performance modeling. It has the capability to model complex thermo-mechanical behavior from both discrete and smeared pellet fuel meshes, the fuel-cladding gap and plenum, and the evolution of various fuel and cladding materials over their operation.

The constitutive relations used in this analysis under normal operating conditions for FeCrAl and Zircaloy cladding are documented in previous analyses (Sweet et al., 2018; Sweet et al., 2016), and reflect the C35M FeCrAl alloy and Zircaloy-4. Because SiC/SiC cladding is expected to exhibit substantially less oxidation (Koyanagi et al., 2017) as well as thermal (CARTER et al., 1984) (< 1673K) and irradiation-induced creep deformation (Katoh et al., 2013), only fundamental thermo-elastic properties and irradiation swelling are considered for this cladding material.

For the elastic modulus, an orthotropic stiffness tensor is described using: $E_{\theta,r} = 243$ GPa (Jacobson et al., 2016), $E_z = 205$, $\nu_{\theta,r} = 0.21$, and $\nu_z = 0.17$ (Singh et al., 2018a). Where E is the Young's modulus and ν is the Poisson's Ratio, in cylindrical coordinates. Additionally, thermal expansion, thermal conductivity, specific heat, and irradiation swelling are implemented according to a previous parametric evaluation on SiC/SiC cladding performance (Singh et al., 2018b). Unlike the metallic FeCrAl and Zircaloy cladding materials, SiC/SiC composite cladding is very brittle, and, as such, does not undergo much plastic deformation before failure. In this analysis, the failure criteria for SiC/SiC is determined to be the proportional limit strength, conservatively set at 100MPa (Koyanagi et al., 2017). In future analyses, however, the failure criteria might be more accurate if it is implemented by using the statistical strength of the material, such as Weibull failure probability model.

2.1 High-Temperature Constitutive Models

In order to assess the condition of the cladding materials under LOCA conditions, high-temperature (< 2000K) behavioral models were developed as needed and implemented into BISON. These models for Zircaloy and FeCrAl include high-temperature thermal creep, plasticity, failure, and oxidation. Additionally, the models were evaluated against data from cladding burst tests to assess their accuracy.

2.1.1 High-Temperature Thermal Creep Model

For these simulations, both the FeCrAl and Zircaloy cladding utilize two separate models for the thermal creep calculation. These models use a separate calculation during lower temperature steady-state conditions, and under transient conditions, transition into high-temperature models.

For the FeCrAl cladding, the Arrhenius-based relationship describing the C35M thermal creep behavior is used, which is recommended for temperatures up to 870 K ([Field et al., 2017](#)). Above 900 K, the creep relation described by Saunders et al. for Fecralloy is used ([Saunders et al., 1997](#)). To transition between the high and low temperature creep relations, an additional Arrhenius-based relation has been fit and implemented. This transition function is used to ensure that the creep calculation remains a continuous function and does not hinder code convergence. Equation 1 shows the general form of the thermal creep equation used in these calculations. Tabulated values used in the thermal creep calculation for FeCrAl cladding are shown in Table 1.

$$\epsilon_{c,th} = C \cdot \sigma^n \cdot \exp\left(-\frac{Q}{kT}\right) \cdot t \quad (1)$$

where C is the creep pre-exponential ($s^{-1}Pa^{-n}$), σ is the effective stress (Pa), n is the stress exponent fitting parameter, Q is the creep activation energy (eV), T is the temperature in K, t is the time in seconds, and k is the Boltzmann constant ($eV\cdot K^{-1}$). Figure 2 shows the distinct increase in the thermal creep rate corresponding to the high-temperature regime for three varying stresses. Because the same stress exponent is used at all temperatures, the stress scaling between the curves remains constant.

Table 1. Thermal Creep Parameters for FeCrAl Cladding

Cladding Temperature (K)	Creep Prefactor, A ($Pa^{-n}\cdot s^{-1}$)	Activation Energy, Q (eV)	Stress Exponent, n (unitless)
≤ 860	2.89e-36	2.560	
$860 < T < 890$	2.20e-12	6.635	5.5
≥ 890	5.96e-27	4.062	

Similarly, for the Zircaloy cladding, the Limback thermal creep model ([Limbäck and Andersson, 1996](#); [Sweet et al., 2018](#)) is used up to 700 K. Above 900K, a cladding thermal creep model derived from cladding tests under LOCA conditions is used, as described by ([Erbacher et al., 1982](#)). Between these temperatures, a weighting term is used to interpolate between the different functions. The LOCA thermal creep model currently implemented in BISON takes the same form as the model for the FeCrAl (Eq. (1)). This model also takes into account the volumetric fraction of the α and β phase in the Zircaloy cladding based on the time and temperature variation rate ([Pastore et al., 2015](#)). Additionally, this calculation also includes an anisotropic reduction factor for the pure α phase ([Erbacher et al., 1982](#)).

Table 2. High-Temperature Creep Parameters for Zircaloy-4 Cladding ([Erbacher et al., 1982](#))
[adapted from ([Pastore et al., 2015](#))]

Zircaloy Phase	Creep Prefactor, A ($Pa^{-n}\cdot s^{-1}$)	Activation Energy, Q (eV)	Stress Exponent, n (unitless)
α	3.99e-32	$3.33 + 2.56e-4 (T-923.15)$	5.89
α - β (50%-50%)	2.51e-15	1.06	2.33
β	1.65e-22	1.47	3.78

Note: in the mixed α - β phase if the strain rate exceeds $3e-3s^{-1}$, interpolation is performed directly between the individual α and β phases

Figure 2 shows the thermal creep rate for the Zircaloy and FeCrAl cladding materials from 600 K – 1220 K for increasing stresses. This considers only the pure α -phase Zircaloy thermal creep constants. Zircaloy exhibits much more thermal creep at lower temperature, and this trend does persist with increasing temperature, although with a decrease in the difference between the thermal creep rates of Zircaloy versus FeCrAl. As the temperature reaches nearly 1200 K, the thermal creep rate for the FeCrAl is about an order of magnitude less than Zircaloy. This shows the Zircaloy cladding will experience much more thermal creep deformation than the FeCrAl cladding over burst relevant conditions.

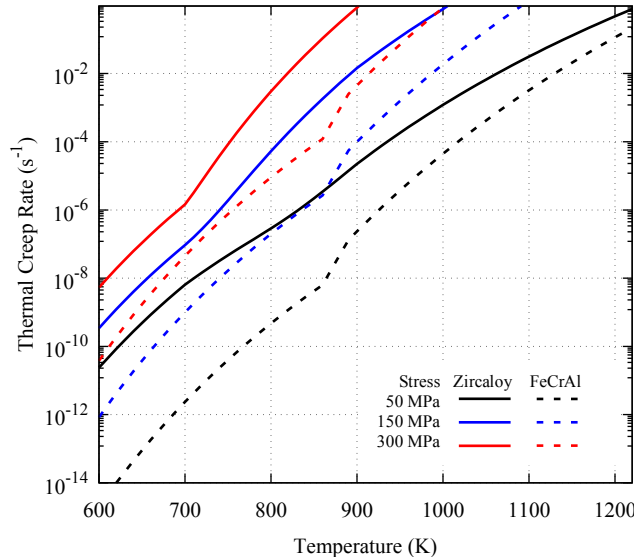


Figure 2. The thermal creep behavior for both the FeCrAl and the Zircaloy is divided into a separate low-temperature and high-temperature contribution with interpolation between the two regions.

2.1.2 Cladding Plasticity and Failure Models

In order to calculate the plastic deformation and assess failure of the cladding materials, isotropic plasticity models are used to define the stress-strain relationship after the material reaches the yield point. For this analysis, data from FeCrAl material testing ([Maloy et al., 2016](#); [Yamamoto et al., 2015](#)) is used to develop a power-law strain hardening model which is implemented into BISON. The ultimate tensile strength is used as the failure criteria for the FeCrAl cladding. As the strain progresses beyond the yield point of the material, the simulations will eventually reach the failure criteria; when this stress is reached, the simulation is terminated. This is based on observations from prior burst testing experiments where very little necking occurs in the cladding before rupture ([Massey et al., 2016](#)). The yield strength and ultimate tensile strength of FeCrAl are detailed in ([Yamamoto et al., 2015](#)). Both the yield and ultimate strength begins to rapidly decrease as the temperature approaches $\sim 2/3$ of the alloy melting temperature. For this analysis, the C35M (Rolled) properties are used to simulate the FeCrAl cladding.

In order to utilize this method of cladding failure, the uniform plastic elongation was obtained from an similar FeCrAl sample ([Maloy et al., 2016](#)) and used to derive a series of power-law strain

hardening relations for the alloy at several different temperatures. These relations were implemented into BISON and interpolated to provide a more thorough description of the temperature-dependant plastic behavior of the FeCrAl cladding. This model does not consider any change in the yield strength or ultimate tensile strength due to irradiation hardening. While irradiation hardening is known to increase both the yield and tensile strength at reactor operating temperatures (Field et al., 2017), assessing the appropriate values to use during an accident is complicated by the anticipated thermal annealing of the irradiation damaged microstructure.

To demonstrate the power-law strain hardening model and FeCrAl cladding failure criteria, a rudimentary simulation of a tension test was performed in BISON for the FeCrAl alloy. This tests consists of a coarse finite-element tensile specimen where the bottom is fixed and the top of the test specimen is subject to a slowly increasing strain. This places the specimen in uniaxial tension, and the yield and subsequent failure of the material can be modeled, as shown in Figure 3. In this simulation, the tensile test was performed at four separate temperatures ranging from room temperature to the approximate cladding rupture temperature expected during a LOCA. These simulations end with assumed cladding failure at the calculated ultimate tensile strength. The results of these BISON modeled tensile tests show a decreasing yield strength and ultimate tensile strength with increasing temperature and show the variation in uniform elongation of the alloy, expected at cladding failure.

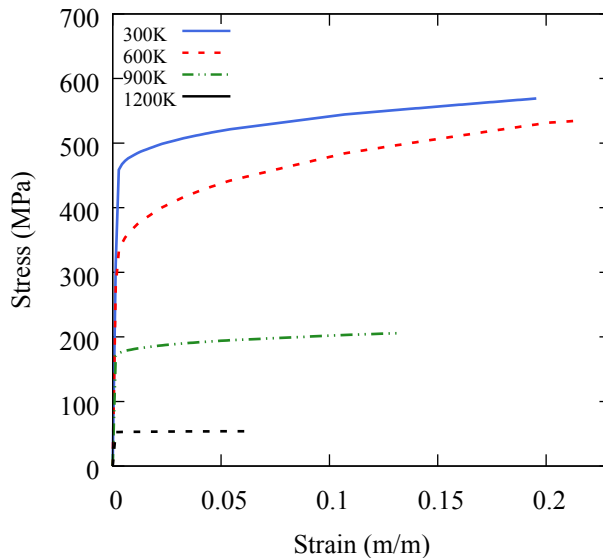


Figure 3. BISON model predictions for the stress strain response of a FeCrAl subject to a simulated tensile test, as a function of test temperature. These simulations end when the ultimate tensile strength is reached.

In order to better predict the high-temperature failure of the FeCrAl cladding, the ultimate tensile strength of the alloy was re-examined. This was motivated by a lack of data at higher temperatures where the alloy is expected to lose strength much faster than a simple linear interpolation to the melting temperature would predict. Figure 4 shows the ultimate tensile strength implemented into BISON. This shows that above 1000 K there is no data, so the expected behavior of the alloy must be used. In the first iteration of this model, the ultimate

tensile strength was simply interpolated to the melting temperature where the alloy is assumed to have no remaining strength (~1773K). This results in an overprediction of the ultimate tensile stress. Next, the ultimate tensile strength was estimated based on the high temperature performance of stainless steels, which lose much of their strength before the alloy reaches the melting temperature. This estimation is used in the current analysis and provides a simple model for the cladding failure.

This was compared against a recent fit of Pint’s (Pint and Baldesberger, 2018) data for the C26M alloy. This fit takes the same functional form as the burst stress used later for the Zircaloy, and it appears to predict a larger ultimate tensile strength, which may lead to a longer time before cladding rupture than the fit used in this analysis. For future analyses concerning the C26M alloy, it is recommended to use a similar fit, as shown in Fig.4. While this is an early implementation for the failure criteria of FeCrAl cladding, a more thorough examination of the material behavior at high temperatures could be made with more ultimate tensile strength data.

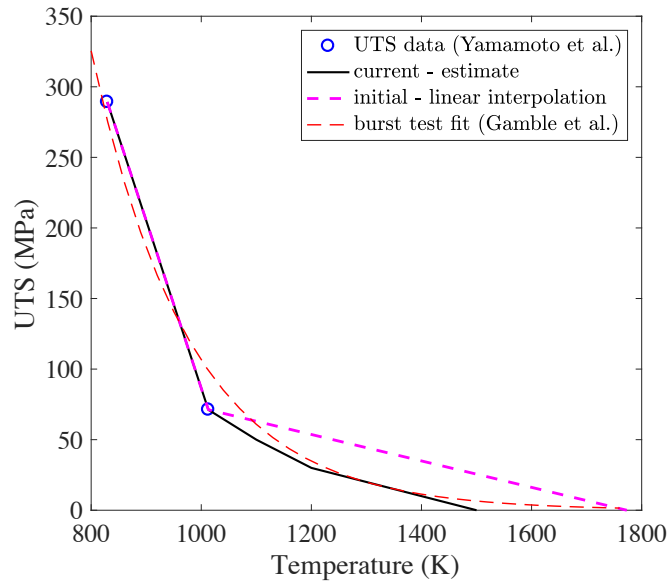


Figure 4. Ultimate tensile strength of FeCrAl as a function of temperature showing two iterations of the model implemented in BISON for high temperatures (initial versus current), compared to a fit to available data performed by Gamble and co-workers (Gamble et al., 2017) and UTS data from (Yamamoto et al., 2015).

To calculate the plastic behavior of the Zircaloy cladding, a much more thorough model, the PNNL stress-strain correlation, developed at Pacific Northwest National Laboratory for the FRAPCON fuel performance code (Geelhood et al., 2008), is currently implemented in BISON (Hales et al., 2014) and used for this analysis. This model utilizes a strain-rate dependent strain hardening model with a variable (temperature, cold work, compositions, etc.) strain hardening exponent and strength coefficient to predict the Zircaloy response at higher fuel burnups.

Failure of Zircaloy cladding is determined from burst stress data that was developed from the REBEKA burst test experiment (Erbacher et al., 1982), in addition to a strain rate failure criteria

for low-stress failure. This burst stress function is shown in Equation 2, and is dependent of the cladding phase, temperature, and the fraction of oxygen dissolved into the cladding.

$$\sigma_B = a \cdot \exp(-bT) \cdot \exp\left(-\left(\frac{f_{wt,ox} - 0.0012}{9.5 \cdot 10^{-4}}\right)^2\right) \quad (2)$$

Where σ_B is the cladding burst stress in MPa, a and b are burst stress parameters (shown in Table 3) based on the phase of the Zircaloy, T is the temperature in K, and $f_{wt,ox}$ is the weight fraction of oxygen dissolved in the cladding. In this expression, the initial oxygen weight fraction of the cladding is assumed to be 0.0012. In BISON, the oxygen weight fraction in the cladding is calculated from the oxygen mass gain from the cladding oxidation model. As previously mentioned, the Zircaloy phase fraction is calculated using a separate model in BISON ([Pastore et al., 2015](#)).

Table 3. Phase Dependent Burst Stress Parameters for Zircaloy-4 ([Erbacher et al., 1982](#))

Phase	a (MPa)	$b \times 10^3$ (K ⁻¹)
α	830	1.0
α - β (50%-50%)	3000	3.0
β	2300	3.0

At high temperatures, the zircaloy cladding experiences a large thermal creep strain rate which allows the alloy to undergo significant stress relaxation such that the burst stress cannot be reached. Because this model may not accurately assess the cladding failure in low-stress conditions, an additional strain-rate failure criterion ($\dot{\epsilon}_B = 2.78 \cdot 10^{-2} \text{ s}^{-1}$) is used ([Hales et al., 2014](#); [Pastore et al., 2015](#)). It has also been suggested to include a limiting strain along with the strain rate criteria ([Van Uffelen and Suzuki, 2012](#)), and although this is not included here, it will be examined as this work is extended. As previously noted, the failure criteria for SiC/SiC is defined as the proportional limit strength, which, in this case, is assumed to be ~100 MPa.

2.1.3 Oxidation Models

The oxidation behavior for Zircaloy and FeCrAl cladding has been implemented into BISON in order to calculate the weight gain of oxygen in the cladding, the thickness of the oxide layer on the cladding, and the thickness of the metal consumed. For the Zircaloy and FeCrAl cladding, a low temperature and high temperature oxidation model is included.

The high temperature data for the FeCrAl cladding is based on measurements of the Kanthal APMT alloy, which have been modified using a scale factor to adjust for the alloy composition ([Field et al., 2017](#)). This work details the result of a series of oxidation tests carried out in 1200°C steam for a variety of compositions of FeCrAl alloys, with varying chromium and aluminum content. For the expected alloy (>10% Cr 5-6% Al), a scale factor of 2.3 is used and assumed to be conservative.

In order to simulate FeCrAl in the BWR environment, data is used from an investigation of the oxidation of an Fe-13Cr-4Al alloy in hydrogen water chemistry ([Terrani et al., 2016](#)). The high temperature and low temperature relations are then connected as the high-temperature reaction is extended down to 1173K and the low-temperature is interpolated using an Arrhenius relation from the single present data point to the lowest high-temperature point. This is interpolated to the lowest temperature where alumina is expected to become the dominant oxidation layer formed ([Engkvist](#)

[et al., 2010](#); [Rybicki and Smialek, 1989](#)). Without much data in the intermediate temperature region, it is difficult to determine the accuracy of this assumption, however, the oxidation rate constants indicate that, even at elevated temperatures, much less oxidation is expected than for Zircaloy.

To simulate the Zircaloy cladding for low temperatures, linear oxidation kinetics are considered and implemented using a specific model for a boiling water reactor ([Lanning et al., 1997](#)). This model uses linear kinetics because it assumes that the transition thickness from cubic to linear scaling is negligible. It should be noted that this BWR specific model predicts significantly less mass gain than corresponding models for PWRs, consistent with the lower cladding temperatures in a BWR.

At higher cladding temperatures (>673 K) the Leistikow et al. ([Leistikow et al., 1983](#)) oxidation model is implemented as described by Pastore and Shanz, respectively ([Pastore et al., 2015](#); [Schanz, 2003](#)). To provide a conservative estimate of the oxide formation after increasing past the normal operating temperatures, this model is extended to lower cladding temperatures than originally intended (~873K).

2.2 LOCA Operating Conditions

In order to simulate the LOCA, representative boundary conditions are applied to the axisymmetric fuel rod geometries described in, reviewed in Table 4. These fuel rod designs are estimates of those from a BWR/4 which have been modified due to limited data and, in the case of the FeCrAl clad fuel rod, to account for the parasitic neutron absorption for the cladding alloy.

The postulated accident and associated conditions are derived from a study on the effect of fuel thermal conductivity on the temperature progression of the fuel and cladding during a LBLOCA in a BWR ([Terrani et al., 2014](#)). For this accident scenario, there is an assumed double-ended guillotine break in the coolant pipe between the pressure vessel and the recirculation pump isolation valve. The onset for this accident is actuated at three separate fuel burnups to determine the sensitivity of the cladding behavior to the integral fuel rod state. The power production for this fuel rod is controlled with a power history and axial power profile, while the cladding temperature is controlled by the coolant temperature and coolant heat transfer coefficient. The reactor is operated using steady state conditions until the accident is initiated at the time of 0s. Here, the recirculation pipe is assumed to be broken and the reactor is scrammed. As power in the core is reduced and the recirculation pumps slowly blowdown, the cladding temperatures initially decline. However, as the coolant flow slowly stagnates, the cladding temperatures begin to rise. The low-pressure coolant injection system is actuated at ~91s and eventually quenches the core.

Table 4. Fuel geometry specifications for 2D axisymmetric fuel performance analyses.

Cladding Material	Fuel Radius (μm)	Gap Thickness (μm)	Cladding Thickness (μm)	Fuel Length (m)	Cladding Length (m)	Enrichment (% U-235)
Zircaloy	4400	100	600			4.11
SiC/SiC	4400	100	600	3.66	4.08	4.11
FeCrAl	4700	100	300			4.68

- This produces a total outer radius of 5100μm for all three cladding types.

In order to determine the difference in cladding performance during the unmitigated accident, these simulations do not consider the initiation of the low-pressure coolant injection system; the fuel rod temperatures are allowed to increase until cladding failure consistent with a beyond design basis accident scenario.

The power history and axial power profile used in this analysis is shown in Figure 5. The fuel rod power ramps up to steady-state operation at 18 kW/m over 100 hours and held constant until the designated burnup is reached. At the onset of the accident conditions, the reactor core is scrammed and the fuel power is reduced. Equation 3 is used to calculate the assumed power production due decay heat ([El-Wakil, 1978](#)).

$$Q_{decay} = 9.5 \times 10^{-2} \cdot Q_0 \cdot t^{-0.26} \quad (3)$$

Where Q_{decay} is the decay heat production in the fuel (kW/m), Q_0 is the steady state heat production (in this case 18 kW/m), and t is the time after the reactor scram (seconds). While this is not the most accurate calculation for decay heat production, it does provide a representative value, which, for this particular case this leads to ~ 2 kW/m after the reactor scram. The axial power profile, shown in Figure 5(b) remains static in these calculations. As discussed later, this concentrates the fuel burnup to the center of the fuel rod, leading to considerably higher temperatures, greater burnup, and during the transient, even greater decay heat production.

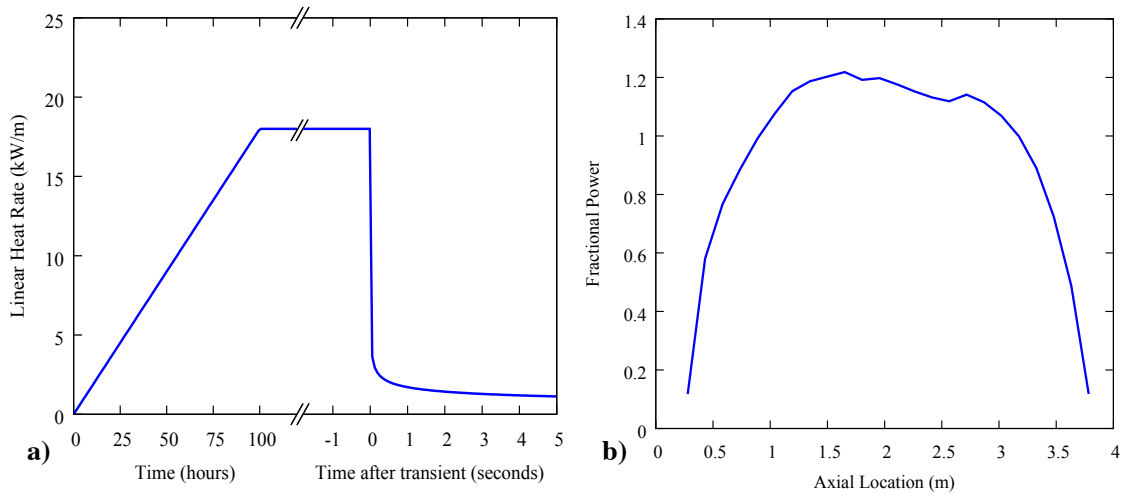


Figure 5. The power history of fuel rods in this LOCA analysis, (a) the Linear heat rate is divided into three regions: the initial ramp to operating power, constant operation at 20kW/m, and the reactor scram at the beginning of the transient conditions and the subsequent decay heat production. The axial power profile (b) is assumed to be constant for all three regions.

Pertinent reactor and fuel rod properties and typical for a BWR, are summarized in Table 5.

Table 5. Loss-of-Coolant Accident Reactor and Fuel Properties

Parameter	Value	Unit
Coolant Pressure	7.136	MPa
Initial Plenum Pressure	0.5	MPa
UO ₂ Density	95%	T.D.

3. RESULTS

3.1 Steady-State Operation Results

For these simulations, before the onset of the transient conditions, the fuel is operated to two specified burnups, namely, 20 MWd/kgU and 40 MWd/kgU. Although more comparisons were planned at different burnups, convergence issues in several of the simulations prevented them from providing meaningful data. This is performed to compare the accident progression and failure of the three cladding types as a result of the fuel rod state (temperature, pressure gap thickness, etc.). Because a description of the SiC/SiC ([Singh et al., 2018b](#)) and Zircaloy and FeCrAl ([Sweet et al., 2018](#)) cladding behavior under constant operating conditions is thoroughly discussed elsewhere, only condensed results are presented here.

Figure 6 shows the average fuel centerline temperature (a) and the minimum gap thickness (b) for these fuel rods up to a burnup of 40 MWd/kgU. The sharp, nearly vertical, drops in the fuel temperatures occur quickly during the postulated accident and will be discussed further in the next section. The average fuel centerline temperatures remain similar between the Zircaloy and FeCrAl cladding for much of the simulation. There is a small deviation due to the gap closure behavior between the cladding types. The Zircaloy cladding immediately begins to creep-down, closing the gap and improving the heat transfer across the fuel rod gap. This results in a lower (~50K) average fuel centerline temperature over much of the simulated fuel burnup. The SiC/SiC cladding, however, a much larger expansion of the fuel cladding gap (a combination of irradiation swelling and thermal expansion), and therefore experiences much greater fuel temperatures for much of the simulation.

The gap closure behavior of both cladding materials is shown in Figure 6(b). Although this suggests gap closure occurs at ~22 MWd/kgU and ~39 MWd/kgU for the Zircaloy and SiC, respectively, this effect is localized to the highest power region, as described by the axial power profile. This is a consequence of using a static axial power profile over the entire simulation, and concentrates the neutron flux, burnup, and temperature in a small section of the fuel rod. In this fuel rod section, the fuel expands more thermally and experiences more fuel relocation and fission product swelling. As well, in this location, the cladding experiences more dimensional change due to irradiation (swelling/growth) and irradiation creep deformation. In these simulations, the FeCrAl cladding does not experience gap closure before 40 MWd/kgU.

The maximum oxidation thickness that that forms on the cladding surface is shown in Figure 7. The Zircaloy cladding forms ~15 μm of oxidation by the end of the simulations, while the FeCrAl forms ~3 μm . As previously noted, Zircaloy cladding in the BWR environment is expected for form significantly less oxidation than in the PWR ([Lanning et al., 1997](#)). Because of the linear scaling, the oxidation layer in the Zircaloy continues to grow at a constant rate. For the FeCrAl, however, due to the parabolic kinetics associated with oxide layer formation, the growth rate diminishes with increasing thickness.

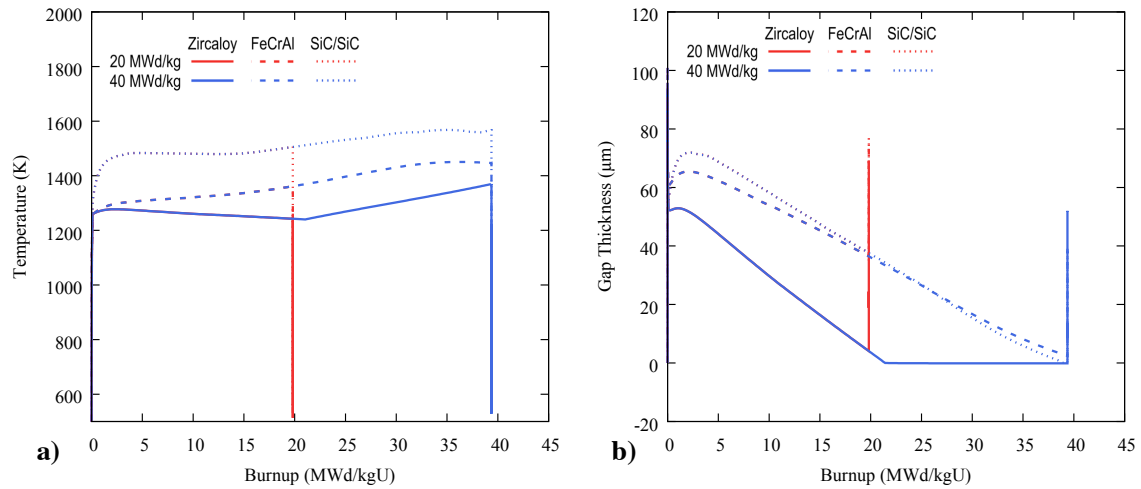


Figure 6. The average fuel temperature (a) for the SiC/SiC cladded fuel rods is much larger (~200 K) for much of the fuel utilization. The onset of gap closure (b) occurs much sooner for the Zircaloy cladded fuel rods than the SiC/SiC, while the FeCrAl cladded fuel rod does not experience gap closure up to 40 MWd/kgU.

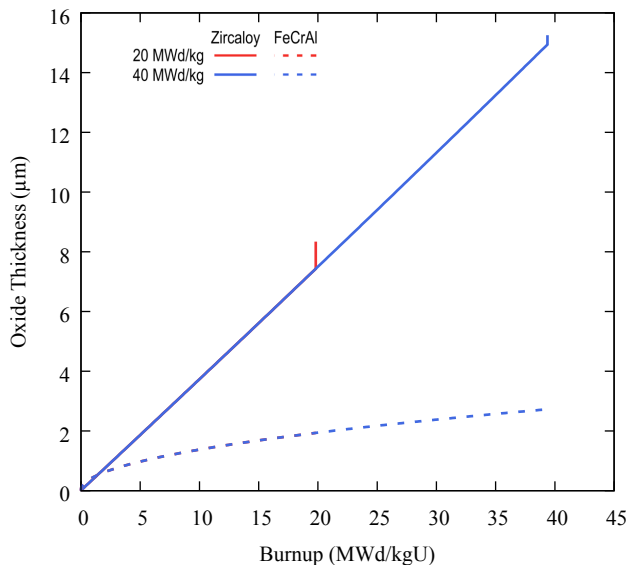


Figure 7. The maximum cladding oxidation thickness for the Zircaloy versus FeCrAl cladding, as a function of burnup.

3.2 LOCA Results

After the steady-state irradiation period, at a specified fuel burnup, the accident conditions are initiated based on the scenario presented in Section 2.2, although this analysis does not initiate the low-pressure injection system at ~91 seconds after the accident. Figure 8 shows the average fuel centerline temperature (a) and the maximum cladding temperature (b) during the transient. In these figures, the reactor is scrammed at 0s, and the reactor power then decays according to the fission product decay heat relation provided in Eq. (3). The coolant flow slowly decreases as the core recirculation pumps stop. As the coolant flow stagnates, the coolant temperatures increase, and the coolant heat transfer coefficient is decreased.

Figure 8(a) shows the variation in the fuel temperatures during the steady-state operation due to the fuel rod condition. After the reactor is scrammed, the fuel temperatures slowly decrease as the heat is removed while the coolant pumps stop. As the coolant stagnates in the core, fuel temperatures begin to rise and, eventually, converge, independent of cladding type.

The peak cladding temperatures (Figure 8(b)) show a similar trend after the accident conditions have been initialized. The cladding temperatures slowly decrease after the reactor has scrammed, reaching a minimum at ~41 seconds. This plot also shows the cladding temperatures from the TRACE simulation that actuated the low-pressure injection at approximately 91 seconds ([Terrani et al., 2014](#)). In the TRACE simulation the cladding temperatures begin to decrease at ~140 seconds as the core is re-flooded. However, in our BISON analysis the temperatures continue to increase until the cladding fails. As previously mentioned, these simulations are terminated when the burst criterion is reached. These results show progressively lower temperatures for the increasing fuel burnups in the FeCrAl and Zircaloy cladded fuel rods. These simulations also show very similar burst times for all three cladding types.

Figure 9 shows the maximum fuel cladding gap thickness (a) and the maximum cladding hoops stress (b) during the accident conditions simulated with BISON. Both of the Zircaloy simulations, along with the SiC/SiC at 20 MWd/kgU experience gap closure by the time the accident conditions are initiated. After the onset of the accident conditions, the fuel cools down and the coolant system pressure rapidly drops. As the fuel contracts and the cladding is expanded due to the change in pressure differential, the fuel cladding gap is reopened. For the Zircaloy, as the fuel rod temperatures begin to increase, the pressure differential between the fuel rod plenum and coolant system allow the fuel cladding to begin rapidly expanding due to thermal creep. The FeCrAl cladding does not experience the same magnitude of thermal creep; the thermal expansion of the cladding and increase in rod internal gas pressure drive the increase in gap thickness. The SiC/SiC cladding does not experience any creep deformation, and the gap expansion behavior appears to be completely driven by the fuel thermal expansion.

Leading up to the accident scenario, the maximum cladding hoop stress (Figure 9(b)) is initially in a tensile state due to mechanical interaction between the fuel and cladding. After the onset of the LBLOCA conditions, the gap is reopened, as the reactor coolant pressure is reduced to atmospheric pressure. This generates significant hoop stresses in the cladding, as the fuel rod plenum pressure begins to increase with the fuel temperatures. In these simulations, the SiC/SiC cladded fuel rods fail at much larger stresses their FeCrAl and Zircaloy counterparts. It should be noted that for 60

MWd/kgU, the SiC/SiC composite cladding failed during normal operation before the onset of the transient conditions. This failure was attributed to PCMI which induced a hoop stress beyond the proportional limit strength.

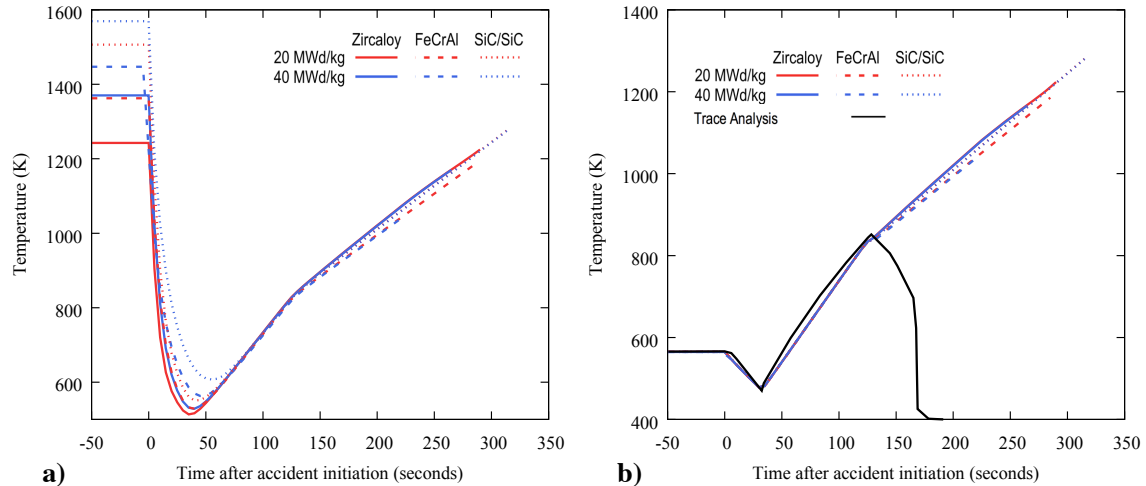


Figure 8. The maximum fuel centerline temperature (a) and the maximum cladding temperature (b) for all three cladding types as a function of time after the accident. The results from the TRACE simulation are (black line) included in b) to provide a comparison.

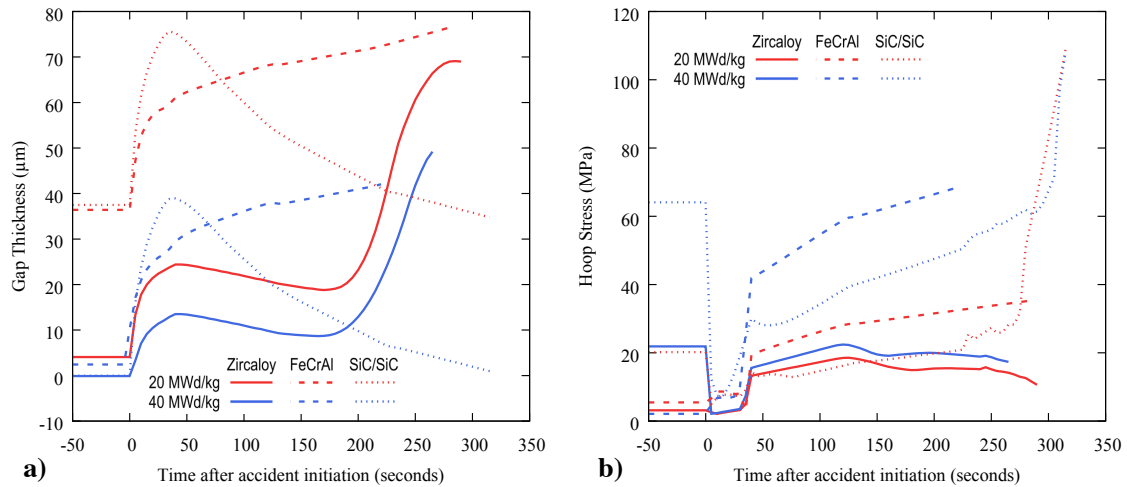


Figure 9. After the reactor is scrammed, the fuel contracts and the fuel cladding gap (a) is expanded. The Zircaloy cladding shows a much sharper increase in the gap thickness as the accident conditions progress. The maximum cladding hoop stress (b) is reduced as the accident conditions are initiated, however, as the accident progresses, the hoop stress in the FeCrAl and SiC/SiC cladding increases until failure.

Leading up to the accident scenario, the maximum cladding hoop stress (Figure 9(b)) is initially in a tensile state due to mechanical interaction between the fuel and cladding. After the onset of the LBLOCA conditions, the gap is reopened, as the reactor coolant pressure is reduced to atmospheric pressure. This generates significant hoop stresses in the cladding, as the fuel rod plenum pressure begins to increase with the fuel temperatures. In these simulations, the SiC/SiC clad fuel rods fail at much larger stresses than their FeCrAl and Zircaloy counterparts. It should be noted that for 60 MWd/kgU, the SiC/SiC composite cladding failed during normal operation before the onset of the transient conditions. This failure was attributed to PCMI which induced a hoop stress beyond the proportional limit strength.

These results show that the SiC/SiC clad fuel rods fail at nearly the exact same time, implying that the failure is related to the cladding temperature. The Zircaloy and FeCrAl cladding materials fail at similar times, however the FeCrAl cladding fails at larger cladding hoop stresses.

4. SUMMARY

This work documents initial efforts to extend the steady-state modeling capabilities established for FeCrAl cladding in the BISON fuel performance code to high temperature transient conditions. In order to compare the behavior of FeCrAl and Zircaloy cladding during a simulated a loss-of-coolant accident, high-temperature constitutive models, failure criteria, and boundary conditions were implemented.

These results show that at lower burnups FeCrAl cladding will generally burst at a similar time and temperature as the Zircaloy cladding under the specific reactor operating and accident conditions that were simulated, but the failure conditions involve reaching larger cladding hoop stresses. With increasing burnup, however, the temperature and time before the FeCrAl cladding ruptures slowly decreases. As expected, the main driving force for differences in burst behavior between the various fuel burnups is the pressure differential across the cladding as the transient conditions evolve. The FeCrAl cladding thickness used in this analysis is thinner than the thickness expected to be deployed in commercial reactors, which would tend to increase the difference in cladding failure time for the FeCrAl rods during the accident. Likewise, the initial model we have implemented for the temperature dependence of the FeCrAl ultimate tensile stress is conservative with respect to the experimentally measured burst strength, as shown in Fig. 4; and implementing an improved model is also expected to increase the time before failure during LOCA conditions.

The SiC/SiC cladding remained integral slightly longer and was predicted to fail at a slightly higher temperature than the other cladding materials considered over the power history and burnups of 20 GWd/tU and 40 GWd/tU. The SiC/SiC cladding experienced failure during LOCA conditions at the same time and temperature, regardless of the fuel rod burnup. This indicates that the material is sensitive to thermal stresses that develop due to differential thermal expansion from temperature gradients across the cladding. At higher burnups, the SiC/SiC cladding is predicted to fail due to PCMI before the onset of the transient LOCA conditions. However, there is uncertainty in the failure strength of the SiC/SiC cladding, and in particular the temperature dependence. The next steps in this analysis involve using statistical methods to determine the failure probability of the cladding and evaluating the post-quench ductility to assess whether a coolable geometry is maintained.

To further enhance this analysis, additional improvements to the FeCrAl and SiC/SiC constitutive models are necessary. The development of the power law strain-hardening plasticity model consisted of a combination of different FeCrAl cladding property tests. Although these tests are conducted on similar alloys, no single test was able to provide a complete description of the temperature-dependent plastic behavior of the FeCrAl alloy. Because of this, it is expected that the behavior of the target alloys will differ from the model that is implemented. Similarly, we have assumed no thermal or irradiation creep for the SiC clad, and have assumed a temperature independent proportional limit stress. The cladding failure models should also be subject to more thorough investigation to determine if strain-based failure models are more applicable. The current burst stress and ultimate tensile strength models lead to situations under low-stress conditions the failure time and temperature are greatly over predicted due to stress relief mechanisms in the cladding.

The operating conditions used in this analysis generate unique results because the fuel burnup is concentrated near the center of the fuel rod due to the static axial power profile. This increases the heat generation due to fission product decay, and subsequently influences the mechanical behavior of the cladding in that region and the cladding oxidation. These simulations also do not contain the axial variation in the coolant temperature typical of a boiling water reactor. Because the temperature profile is constant axially along the fuel rod, the location of the fuel rupture is especially sensitive to the axial peaking factors. For future simulations, a combination of axial power profiles to more evenly distribute the fuel power axially over the fuel rod are expected to provide a more accurate set of conditions to model the accident progression. Coupling to a reactor systems or thermal hydraulics code would better define the cladding temperature evolution under transient conditions and would also allow evaluation of different accident scenarios.

Additionally, neither the thermal or mechanical properties of the cladding oxides have been implemented into these simulations. While the FeCrAl cladding is not expected to develop a significant oxide thickness, Zircaloy cladding will and at the higher temperatures, SiC cladding can be degraded through oxidation and SiO₂ formation. As the cladding is oxidized and the metal is consumed, the cladding is thinned and replaced with a brittle oxide ceramic with lower thermal conductivity. Ongoing work is being performed to incorporate a discrete oxide layer directly into the finite element simulations.

5. REFERENCES

- Carmack, J., Goldner, F., Bragg-Sitton, S.M., Snead, L.L., 2013. Overview of the US DOE accident tolerant fuel development program. Idaho National Laboratory (INL).
- CARTER, C.H., DAVIS, R.F., BENTLEY, J., 1984. Kinetics and Mechanisms of High-Temperature Creep in Silicon Carbide: II, Chemically Vapor Deposited. *Journal of the American Ceramic Society* 67, 732-740.
- Cathcart, J., Pawel, R., McKee, R., Druschel, R., Yurek, G., Campbell, J., Jury, S., 1977. Zirconium metal-water oxidation kinetics. IV. Reaction rate studies. Oak Ridge National Lab.
- El-Wakil, M.M., 1978. Nuclear heat transport. American Nuclear Society.
- Engkvist, J., Canovic, S., Hellström, K., Järnäs, A., Svensson, J.-E., Johansson, L.-G., Olsson, M., Halvarsson, M., 2010. Alumina scale formation on a powder metallurgical FeCrAl alloy (Kanthal APMT) at 900–1,100 C in dry O₂ and in O₂ + H₂O. *Oxid Met* 73, 233-253.
- Erbacher, F., Leistikow, S., 1987. Zircaloy Fuel Cladding Behavior in a Loss-of-Coolant Accident: A Review.
- Erbacher, F., Neitzel, H., Rosinger, H., Schmidt, H., Wiehr, K., 1982. Burst Criterion of Zircaloy Fuel Claddings in a Loss-of-Coolant Accident, Burst Criterion of Zircaloy Fuel Claddings in a Loss-of-Coolant Accident.
- Field, K.G., Snead, M.A., Yamamoto, Y., Terrani, K.A., 2017. Handbook on the Material Properties of FeCrAl Alloys for Nuclear Power Production Applications.
- Gaston, D., Newman, C., Hansen, G., Lebrun-Grandie, D., 2009. MOOSE: A parallel computational framework for coupled systems of nonlinear equations. *Nucl Eng Des* 239, 1768-1778.
- Geelhood, K.J., Beyer, C.E., Luscher, W.G., 2008. PNNL stress/strain correlation for Zircaloy. Pacific Northwest National Laboratory (PNNL), Richland, WA (US).
- Hales, J., Novascone, S., Pastore, G., Perez, D., Spencer, B., Williamson, R., 2014. BISON theory manual: The equations behind nuclear fuel analysis. Fuels Modeling & Simulation Department, Idaho National Laboratory, Idaho Falls, Idaho.

- Hofmann, P., 1998. Current knowledge of core degradation phenomena, a review. *J Nucl Mater* 270, 194-211.
- Katoh, Y., Snead, L.L., Parish, C.M., Hinoki, T., 2013. Observation and possible mechanism of irradiation induced creep in ceramics. *J Nucl Mater* 434, 141-151.
- Koyanagi, T., Katoh, Y., Singh, G., Snead, M., 2017. *SiC/SiC Cladding Materials Properties Handbook*.
- Lanning, D., Beyer, C., Painter, C., 1997. FRAPCON-3: modifications to fuel rod material properties and performance models for high-burnup application. NUREG0CR-6534 1.
- Leistikow, S., Schanz, G., Berg, H., Aly, A., 1983. Comprehensive presentation of extended Zircaloy-4 steam oxidation results (600-1600 deg. C).
- Limbäck, M., Andersson, T., 1996. A model for analysis of the effect of final annealing on the in-and out-of-reactor creep behavior of zircaloy cladding, Zirconium in the Nuclear Industry: Eleventh International Symposium. ASTM International.
- Maloy, S.A., Aydogan, E., Anderoglu, O., Lavender, C., Yamamoto, Y., 2016. Viability of thin wall tube forming of ATF FeCrAl. ; Los Alamos National Lab. (LANL), Los Alamos, NM (United States); Pacific Northwest National Lab. (PNNL), Richland, WA (United States); Oak Ridge National Lab. (ORNL), Oak Ridge, TN (United States), p. Medium: ED; Size: 35 p.
- Massey, C.P., Terrani, K.A., Dryepondt, S.N., Pint, B.A., 2016. Cladding burst behavior of Fe-based alloys under LOCA. *J Nucl Mater* 470, 128-138.
- Moalem, M., Olander, D.R., 1991. Oxidation of Zircaloy by steam. *J Nucl Mater* 182, 170-194.
- Pastore, G., Novascone, S., Williamson, R., Hales, J., Spencer, B., Stafford, S., 2015. Modeling of fuel behavior during loss-of-coolant accidents using the BISON code, 2015 LWR Fuel Performance Meeting—Top Fuel, Zurich, Switzerland.
- Pint, B.A., Baldesberger, L.A., 2018. Steam Oxidation and Burst Testing in the Severe Accident Test Station. ; Oak Ridge National Lab. (ORNL), Oak Ridge, TN (United States), p. Medium: ED; Size: 10 p.
- Rybicki, G.C., Smialek, J.L., 1989. Effect of the θ - α -Al₂O₃ transformation on the oxidation behavior of β -NiAl + Zr. *Oxid Met* 31, 275-304.

- Saunders, S.R.J., Evans, H.E., Li, M., Gohil, D.D., Osgerby, S., 1997. Oxidation growth stresses in an alumina-forming ferritic steel measured by creep deflection. *Oxid Met* 48, 189-200.
- Schanz, G., 2003. Recommendations and supporting information on the choice of zirconium oxidation models in severe accident codes.
- Singh, G., Gonczy, S., Deck, C., Lara-Curzio, E., Katoh, Y., 2018a. Interlaboratory round robin study on axial tensile properties of SiC-SiC CMC tubular test specimens. *International Journal of Applied Ceramic Technology*.
- Singh, G., Sweet, R., Brown, N., Wirth, B., Katoh, Y., Terrani, K., 2018b. Parametric Evaluation of SiC/SiC Composite Cladding with UO₂ Fuel for LWR Applications: Fuel Rod Interactions and Impact of Nonuniform Power Profile in Fuel Rod. *J Nucl Mater* 499, 155-167.
- Sweet, R., George, N., Maldonado, G., Terrani, K., Wirth, B., 2018. Fuel performance simulation of iron-chrome-aluminum (FeCrAl) cladding during steady-state LWR operation. *Nucl Eng Des* 328, 10-26.
- Sweet, R., George, N.M., Terrani, K.A., Wirth, B., 2016. BISON Fuel Performance Analysis of FeCrAl cladding with updated properties. ; Oak Ridge National Lab. (ORNL), Oak Ridge, TN (United States), p. Medium: ED; Size: 46 p.
- Terrani, K., Pint, B., Kim, Y.-J., Unocic, K., Yang, Y., Silva, C., Meyer, H., Rebak, R., 2016. Uniform corrosion of FeCrAl alloys in LWR coolant environments. *J Nucl Mater* 479, 36-47.
- Terrani, K.A., Wang, D., Ott, L.J., Montgomery, R.O., 2014. The effect of fuel thermal conductivity on the behavior of LWR cores during loss-of-coolant accidents. *J Nucl Mater* 448, 512-519.
- Van Uffelen, P., Suzuki, M., 2012. 3.19 - Oxide Fuel Performance Modeling and Simulations A2 - Konings, Rudy J.M, *Comprehensive Nuclear Materials*. Elsevier, Oxford, pp. 535-577.
- Williamson, R.L., Hales, J.D., Novascone, S.R., Tonks, M.R., Gaston, D.R., Permann, C.J., Andrs, D., Martineau, R.C., 2012. Multidimensional multiphysics simulation of nuclear fuel behavior. *J Nucl Mater* 423, 149-163.
- Yamamoto, Y., Pint, B., Terrani, K., Field, K., Yang, Y., Snead, L., 2015. Development and property evaluation of nuclear grade wrought FeCrAl fuel cladding for light water reactors. *J Nucl Mater* 467, 703-716.